Internal structure in small Au crystals resolved by three-dimensional inversion of coherent x-ray diffraction

G. J. Williams,* M. A. Pfeifer,† I. A. Vartanyants,‡ and I. K. Robinson
Department of Physics, University of Illinois, Urbana, Illinois 61801, USA
(Received 12 October 2005; revised manuscript received 18 January 2006; published 13 March 2006)

Coherent x-ray diffraction (CXD) is a technique which utilizes the favorable coherence properties of an x-ray beam to collect three-dimensional (3D) diffraction data from which the 3D shape of a sample can be determined. The shape of the sample is found by reconstructing the phase of the diffracted wave in the far field using iterative techniques and recognizing the relationship between this complex amplitude and the sample's electron density. We describe the experimental procedure for measuring CXD near a high-angle Bragg peak from a small crystal and report the 3D shape information recovered by overcoming the so-called phase problem. We also describe the reconstruction procedure, including some difficulties encountered therein and the steps taken to ameliorate these problems. In the final reconstruction of the electron density we observe nanometer-scale density variation within the crystal that we attribute to deformation.

DOI: 10.1103/PhysRevB.73.094112 PACS number(s): 61.10.Nz, 42.30.Rx, 68.37.Yz

I. INTRODUCTION

When a small crystal is illuminated by a highly coherent beam of x rays, the diffracted intensity is intrinsically related to the crystal's electron density by the modulus squared of the Fourier transform of the density. One requirement for such a measurement is that a relatively large number of diffracted photons must be detected. Fortunately, this criterion is easily satisfied in modern third-generation synchrotron sources like the Advanced Photon Source. More fundamental to the successful recovery of the three-dimensional (3D) shape of the diffracting crystal is that no measurement is made of the diffracted amplitude directly, only of the intensity. Herein lies the famous phase problem of crystallography: the phase information of the diffracted wave is lost in the measurement.

Given the difficulty inherent in overcoming an inverse problem such as this one, it is reasonable to ask whether the result is worthwhile. Indeed, many of the traditional advantages of x-ray diffraction carry over into this technique. For example, x rays interact very weakly with matter, so that the kinematical approximation remains valid for relatively thick samples. Further, they have very short wavelengths, allowing the potential for atomic scale imaging. Their weak interaction also makes possible 3D imaging, while techniques like scanning electron microscopy and atomic force microscopy remain sensitive only to the surface. In fact, an important advantage over traditional microscopy is that the ultimate resolution is diffraction limited and so does not rely on the ability to focus the beam. A principle advantage over transmission electron microscopy is that sectioning is not required even for metallic samples microns thick. In the context of materials science, the scattering around a high-angle Bragg peak is affected by strain within the crystal and so a microscopic technique based on a measurement of that diffraction will be sensitive to this.

Fortunately, there exists a considerable literature dealing not only with iterative algorithms[1–3] that find a set of phases consistent with the measured magnitude of the amplitude and some real-space constraints, but also of theoretical estimates of the uniqueness of a phase set so recovered[4–6] when one real-space constraint is a finite support. Fundamental to these methods is the proper measurement of the diffracted intensity. Namely, as Sayre[7] recognized, the intensity must be sampled at its Nyquist frequency. This leads to the definition of an "oversampling ratio" σ, such that $\sigma = N/S \geqslant 2$, where N is the number of pixels in the detector and S is the number of pixels the real-space object occupies. This may be derived by means of an equation counting argument[8] or through the recognition that the intensity is the Fourier transform of the autocorrelation, which is typically twice the size of the object, and so sampling the intensity at the Nyquist frequency must "oversample" the amplitude.[9]

As mentioned previously, the problem is thought to possess a unique solution in all but pathologically rare cases[5]—namely, those where the diffracted amplitude is factorizable. Nevertheless, there are classes of function that represent trivial ambiguities. For a given $f(x)$, the functions $f(x+x_0)$, $f(x)e^{i\theta}$, and $f^*(-x)$ have Fourier transforms whose magnitudes are indistinguishable from the magnitude of the Fourier transform of $f(x)$. In the last several years, various experiments have shown the feasibility of this method. In 1999, Miao *et al.*[10] reported the recovery of a 2D noncrystalline sample. Robinson *et al.*[11] recovered the 2D projection of the shape of Au crystal using diffraction around a $(11\bar{1})$ Bragg peak. The first successful 3D test object was recovered shortly thereafter,[12] and the recovery of the 3D shape of a Au crystal was reported by the authors in a previous Letter.[13] Other systems, including Au balls[14] arranged in various patterns, have been explored using coherent diffractive imaging.

In the earlier Letter, we presented a method for recovering the 3D shape of a small crystal from a coherent x-ray diffraction (CXD) pattern. The method has the benefit of requiring only slight angular motions to measure the 3D diffraction pattern, but can only be used on crystalline samples, as the diffraction pattern must be collected near a high-angle Bragg peak. Another benefit of the method is that since we make our measurement far from the origin of reciprocal space, we

 ©2006 The American Physical Society

can avoid complications due to measurements taken near the direct beam and easily capture the center of the diffraction pattern. The present paper describes in detail the experimental conditions and iterative algorithms used to recover the 3D shape of a Au crystal from diffraction near the $(11\bar{1})$ Bragg peak.

II. EXPERIMENT

The sample preparation began with a (1×1)-cm^2 piece of Si(100) wafer onto which a 300-Å Au film was deposited *in vacuo*. The thermal oxide on the wafer was left intact, providing an amorphous surface for the film growth and preventing chemical reaction between the film and its substrate. After deposition, the substrate was further reduced in size to 2×2 mm^2. This sample was placed into a pseudoisobaric chamber composed of two pieces of cured ceramic and four quartz slides, with the sample positioned in the center of the cube so constructed. The quartz slides were covered with a commercially prepared Au film, which contained a small amount of Cr (to adhere the Au to the substrate). The presence of Cr is not believed to have influenced the evolution of the sample. This chamber was placed into an oven and heated in air to 1050 °C, 14° below the bulk melting point of Au. After 10 h at this temperature, the sample was cooled to 850 °C and held there for another 10 h before it was rapidly cooled to room temperature. The sample was then affixed to the end of a long ceramic post by means of a ceramic adhesive. This post was inserted into a holder that coupled to the goniometer head and held the sample at beam height. A closed steel cylinder with Kapton-covered entrance and exit apertures was connected to the holder by means of four screws. Finally, a halogen light bulb was placed atop the cylinder to act as a heat source. The bulb was placed in a Au-coated reflector and the height of the cylinder was chosen so that the sample was in the focus spot of the light bulb. Using this apparatus on the diffractometer at Sector 33-ID-D of the Advanced Photon Source (APS), the CXD pattern phased in this paper was collected from the sample at 950 °C in a grazing exit geometry. The beam from the undulator at this source provided a transverse coherence length of at least 5 μm. The experiment required monochromatic radiation; the (333) reflection on a Si(111) double-crystal monochromator was employed. Though the longitudinal coherence length was only of order 1 μm, the coherent assumption was not significantly violated because in the reflection geometry the optical path length difference remains small due to the total Bragg angle of the reflection and the micron-scale dimensions of the sample. It is this path length difference that we require to be less than the longitudinal coherence length.

As the film was heated, it dewetted from its substrate and formed small single crystals. If the Au film had been melted, one would expect the sample to become a collection of single crystals with uniform texture over 4π of solid angle; however, this sample was never melted, so as the film dewets, it forms a collection of single crystals with (111) texture. Under this preparation, all of the crystals on the sample will diffract into the specular (111) reflection, but the off-specular (111) reflections will be randomly oriented about the surface normal. By placing a set of roller blade slits in front of the sample, a beam of a few hundred square microns can easily be created. When this sample was illuminated with such a beam, a scan along the powder ring revealed that a $\{11\bar{1}\}$ Au reflection was detected with a frequency of approximately one reflection per degree. Since Au is fcc, the illumination of each crystal will excite three such reflections, so we estimate that 100–120 crystals were illuminated. Given this large separation between reflections, it was possible to select diffraction from a single grain despite the fact that around 100 were illuminated.

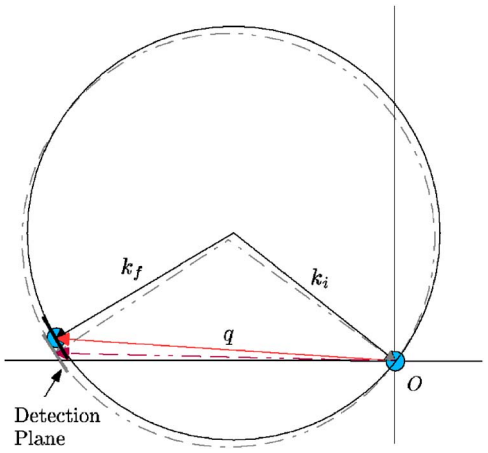

FIG. 1. (Color online) Ewald construction. The solid lines describe the situation at one sample angle and the dotted lines at another as the reciprocal space is moved through the detector plane.

A 2D CXD pattern was measured by positioning a charge-coupled-device (CCD) detector at a Bragg point. This can be visualized as measuring the diffraction into a plane placed tangentially to the Ewald sphere. Two methods of measuring the full 3D pattern immediately present themselves: rock the sample, thereby changing the direction of **q**, or change the energy, to shrink or expand the Ewald sphere through the Bragg point. Practically, the latter causes the CXD pattern to "move" up and down on the detector at subsequent steps along the scan. This movement complicates data collection as it requires coordination between the energy scan steps and the detector arm motion. Therefore, we selected the former method, which is illustrated in Fig. 1. The solid lines describe the situation at one step and the dotted lines at another as the reciprocal space is moved through the detector. In this case, steps of only 0.002° were required in the rocking scan. A selection of the 2D CXD patterns collected in this way is shown in Fig. 2.

As a consequence of the selected collection method, adjacent planes in the scan were not parallel; the angle between them was the step size: 0.002°. We neglected this small misalignment, and the 3D array was created by simply stacking the planes and postponing the geometrical correction until—or if—the analysis called for it. The sampling grid in the 2D CXD pattern was nominally uniform in the plane given by the properties of the CCD—principally the 22.5 μm pixel size—the wavelength of the incident radiation, and the detector arm. In the third direction, the spacing

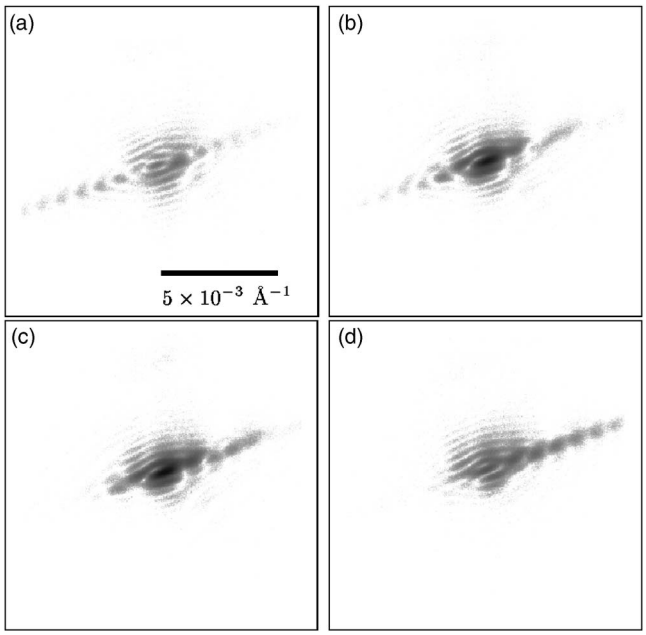

FIG. 2. 2D CXD data collected by rocking the sample. The slices shown are separated by 2×10^{-4} Å^{-1} corresponding to rocking the sample by 0.002°. The CXD pattern has a long diagonal flare indicating a relatively sharp face and the fringe spacings give the approximate size of the sample. While the pattern is not necessarily symmetric in any plane except the one containing the Bragg point, it is centrosymmetric in the sense that the strong flare switches from left to right as one moves through the Bragg point in the third direction. The images are logarithmically scaled.

was uniform but not the same as the 2D measurement and depended upon the rocking step size and the momentum transfer. In the case of a $(11\bar{1})$ reflection from Au illuminated with 9.5-keV x rays measured at 2.93 m, the momentum transfer subtended by a pixel is $\Delta q_{px}=4\times10^{-5}$ Å^{-1} and the step in the third direction was $\Delta q_{\perp}=9\times10^{-5}$ Å^{-1}, giving an anisotropy in the sampling. In the plane of the detector, the q subtended by the lateral extent of a pixel was integrated into a single point with such integrated regions separated by a small fraction of a pixel. In the third direction, there was some integration based on the sensitive region within the CCD device, but the separation between sampling points was dependent upon the scan step size.

III. ITERATIVE METHODS

In order to recover the complex amplitude of the diffracted wave whose intensity was measured as described above, we utilized an inversion procedure following a recipe of alternating periods. Each period consisted of a certain number of iterations of a particular algorithm with some constant set of parameters. The algorithms themselves are error reduction[1] (ER), which is a derivative of the original Gerchberg-Saxton algorithm,[2] and hybrid input/output[1] (HIO) due to Fienup. These are iterative algorithms which transform an iterate between real and reciprocal space many times while applying appropriate constraints in each space so that an eventual solution will be found by identifying an iterate which simultaneously obeys both constraints. They possess the following structure: (i) begin with the measured magnitude of the diffracted amplitude—the Fourier modulus constraint—and assign a random "phase" to each point making it a complex quantity, (ii) Fourier transform this array to form a real-space estimate of the sample's density, (iii) apply a real-space constraint—which will be described below—according to the algorithm in use, (iv) back transform the real-space object forming an estimate of the diffracted amplitude, and (v) replace the magnitude of the amplitude of the estimated diffraction with the measured modulus. Steps (ii)–(v) are then repeated until an acceptable solution is found. ER and HIO differ in the approach taken in enforcing the real-space constraint. The rationale behind alternating between ER and HIO lies in the well-known behavior of ER to stagnate. We found that combining the two sped the convergence to a solution and improved the reproducibility thereof compared to ER or HIO only approaches.

In the case of ER, an iterate $g_{k+1}(x)$ is formed from the real-space estimate $g'_k(x)$—formed by applying the Fourier modulus constraint to $g_k(x)$—by means of the following rule:

$$g_{k+1}(x) = \begin{cases} g'_k(x) & \text{if } g'_k(x) \in S, \\ 0 & \text{if } x \notin S, \end{cases} \tag{1}$$

when only a support is enforced—that is, S is the set of all possible values at all allowed pixels—this has a very straightforward interpretation: at all positions in the array outside the allowed region—the "support"—the density is set to zero. In practice, we also apply a real positive constraint that effectively projects the complex density at all points within the support to the real axis, if positive, and sets all other points to zero. Compound constraints of this nature are perhaps better discussed in the language of projection operations[15,16] whereby the act of enforcing a particular constraint is thought of as projecting the iterate onto the set of all vectors obeying that constraint. If one were to create such an operator from Eq. (1)—say, π_s—then its application could be rewritten as $\pi_s\rho$ where ρ is a vector of dimension equal to the number of elements in the array. Similarly, the Fourier modulus constraint can be written as $\tilde{\pi}_m$, but since all ρ are in real space, we really want $\pi_m=\mathcal{F}^{-1}\tilde{\pi}_m\mathcal{F}$ so that the iterate is Fourier transformed to reciprocal space before application and back to real space afterwards. Then, the action of the algorithm during one iteration can be written as

$$\rho_{k+1} = \pi_s\pi_m\rho_k, \tag{2}$$

where $\pi_m\rho_k$ is what was called $g'_k(x)$ above. Written in this way, it becomes obvious that the procedure is a method of alternating projections.

HIO differs from ER in that it provides an element of feedback by including a portion of the iterate arrived at in the preceding iteration, $g_k(x)$, in the estimate arrived at by application of the Fourier modulus constraint, $g'_k(x)$, and is generally stated[17]:

$$g_{k+1}(x) = \begin{cases} g'_k(x) & \text{if } g'_k(x) \in S, \\ g_k(x) - \beta g'_k(x) & \text{if } g'_k(x) \notin S, \end{cases} \quad (3)$$

where S again represents the support region and β is a scalar, generally chosen to be near one. In analogy to the above discussion of projection operators, one can write the iterate ρ_{k+1} arrived at by means of HIO as

$$\rho_{k+1} = [1 + (1+\beta)\pi_s\pi_m - \pi_s - \beta\pi_m]\rho_k. \quad (4)$$

This has been recognized as a particular case of a more general algorithm, the "difference map," due to Elser.[15]

The progress of an iterate is monitored by means of the quantity

$$\chi^2 = \frac{\sum_{i=1}^{N} (|A_i^{calc}| - \sqrt{I_i^{meas}})^2}{\sum_{i=1}^{N} I_i^{meas}}, \quad (5)$$

where A_i^{calc} is the magnitude of the calculated amplitude in pixel i and I_i^{meas} is the measured value at that point on the detector. Due to the feedback in the application of the real-space constraint during HIO, this metric is unsuitable,[17] so we instead use

$$\chi^2_{\mathrm{Re}} = \frac{\sum_{x=1}^{N} |g_k(x) - g'_k(x)|^2}{\sum_{i=1}^{N} I_i^{meas}}, \quad (6)$$

where the difference is between the iterate in real space before and after application of the real-space constraint. A third quantity is useful in measuring the agreement between estimates:

$$\xi_a^b = \frac{\sum_{x=1}^{N} |g'^{(a)}(x) - g'^{(b)}(x)|^2}{\sum_{i=1}^{N} I_i^{meas}}, \quad (7)$$

where $g'^{(a)}(x)$ and $g'^{(b)}(x)$ are two results of the application of a fitting recipe to different sets of random starting phases. This may be regarded as a measure of reproducibility, where a value of zero would be absolute agreement of the final estimates.[18,19]

We have found during application of these procedures to real data the formation of significant numbers of "vortices"[20] in the reciprocal-space image. These phase singularities are artifacts induced by the original random set of phases assigned to an iterate while fitting data with noise. They can also appear in simulations when the simulated diffraction pattern is noisy and poorly background subtracted. Their designation as an artifact is supported by the observation that two fits with different starting phase sets do not generally have vortices in the same location. These vortices tend to appear in pairs of opposite chirality and may migrate in the reconstruction during the fitting. The problem has been previously addressed where it was recognized by its typical effect on the real-space result: a series of stripes with period related to the distance between vortices via the Fourier relation: $\Delta x \Delta q_x = 2\pi$, where x and q are the real- and reciprocal-space coordinates. Seldin and Fienup[20] have proposed several methods for dealing with these stripes. We have developed a related method that identifies the singularities in reciprocal space and removes them by randomizing the phase over a surrounding patch. The radius of the patch is chosen so that vortices of opposite chirality will be encompassed and annihilated. Our method allows the removal to occur without need for a second iterate and allows the eventual comparison of final estimates without fear of having contaminated them.

In 2D, vortices are easily identified by a vanishing amplitude and a characteristic circular evolution of the phase by integer multiples of 2π around the minima. In 3D, vortices take the form of loops through the 3D space and our earlier strategy for annihilation was not useful. Figure 3 shows three views of vortices detected in 3D. The singularities were detected by searching for points of very rapid phase evolution. Setting this threshold at 0.6 rad provided good agreement with manual examination of a typical reconstruction and the loops are readily apparent. Fortunately, while in 2D a mixture of ER and HIO will stagnate with singularities in the reciprocal space, this was found not to happen in 3D. Figure 4 details the evolution of the vortex structure while the fit to a 3D array is progressing. The 15th slice of the 3D array is shown. The frames shown represent the vortices detected in reciprocal space during a fitting recipe of many alternating periods of ER and HIO. The slice shown in Fig. 4(a) is from the 40th iteration and the frames are shown every 60 iterations thereafter. The recipe was such that (a), (b), (d), (e), and (i) were during ER and the other during HIO. While some vortices annihilate during ER, that algorithm alone was always found to stagnate. A recipe using HIO in addition, however, was found to lead to a vortex-free final estimate without combining iterates. The sporadic points in (h) are indicative of the large phase changes that can occur in reciprocal space during HIO and do not represent vortices.

IV. RESULTS AND ANALYSIS

The CXD patterns collected in this experiment were cropped to form an array of $440 \times 440 \times 30$. The oversampling ratio was quite large in 2D with about 20 pixels per fringe along the diagonal flare and 10 pixels per fringe surrounding the central maxima. It was more difficult to estimate the oversampling in the third direction, and so the support was allowed to be larger than half the total number of slices, but not more than $1/\sqrt[3]{2}$ times the total number of slices, ensuring that $\sigma_z > \sqrt[3]{2}$. In fact, the reconstructed density presented shortly did fill more than half of the slices in this direction. Using the value of $\Delta q_{px} = 4 \times 10^{-5}$ derived in Sec. II in the Fourier conjugate relationship assuming the real-space object is a Heaviside function it would be expected to have dimensions of about 1×4 μm^2 in the plane. This is clearly a poor assumption, so we choose a rectangular support region of $90 \times 120 \times 20$ pixels, which is a region of about 3.5×4.5 μm^2. Although this seems quite large, we recall that the object will reconstruct on an angle, as indicated by the diagonal flare. As previously mentioned, it is difficult to perform this operation in the out of plane direction; as such, the 20-slice size of the support was chosen after an attempt with only 15 slices failed.

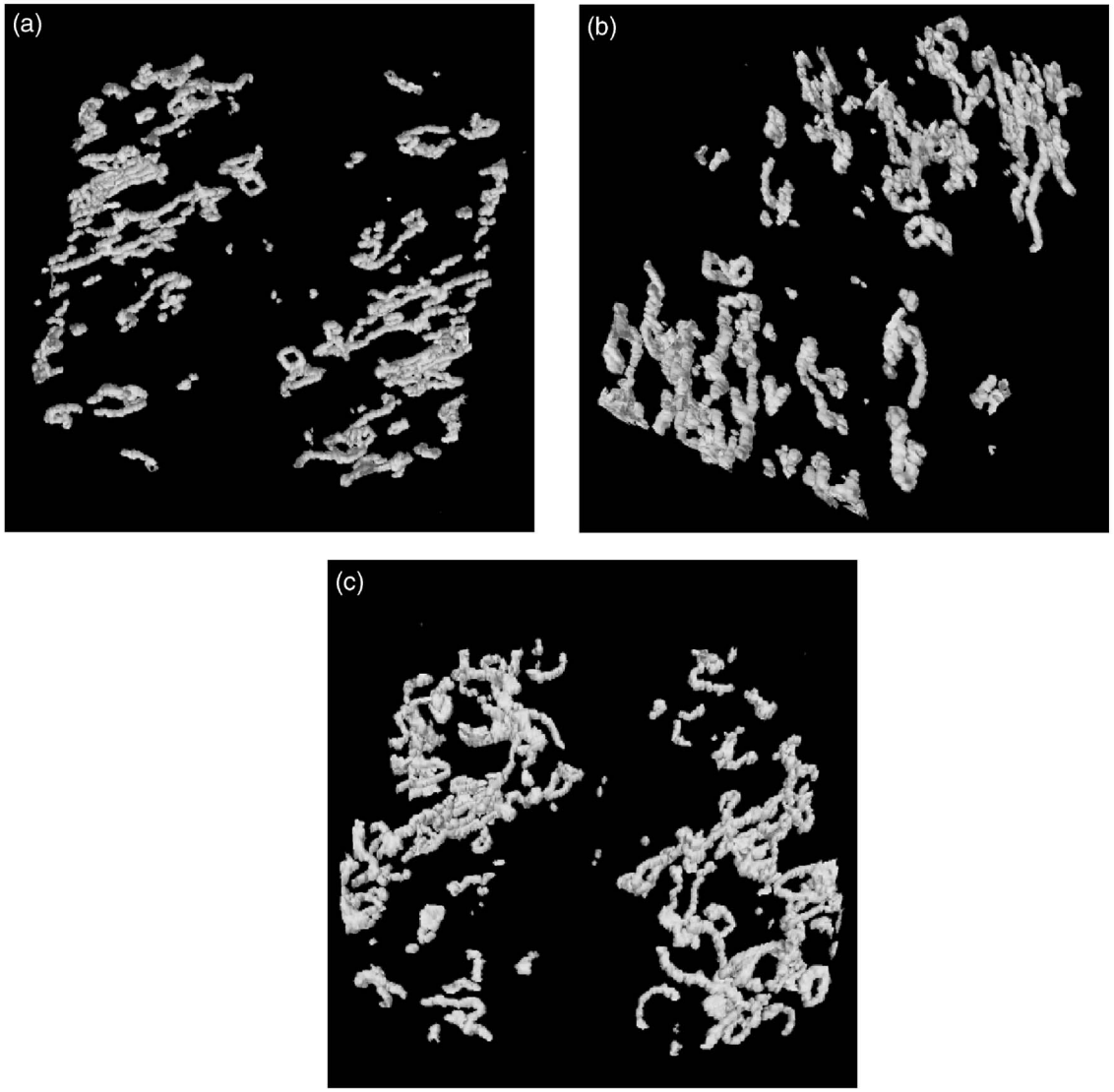

FIG. 3. Three different views of vortices detected in a 3D reciprocal-space reconstruction. (a)–(c) are geometrical projections of the 3D array before application of the Fourier modulus constraint and after, respectively, 150 ER, 100 HIO, and 30 ER iterations showing that the vortices form loops. Since the fast Fourier transform assumes periodic boundary conditions, we see that vortices may extend to the boundary and reappear on the opposite side of the array.

In the case of the data discussed in Sec. II, the fitting recipe consisted of 19 periods of alternating ER and HIO as shown in Fig. 5. ER was performed with a real positive constraint, while HIO utilized only a support constraint. The parameter β was varied between 0.4 and 0.9. Ten sets of random starting phases were used in this run. This calculation took several days to complete on a typical 2.0-GHz personal computer. Of those ten sets, the best two results had $\chi^2_{\mathrm{Re}}=0.0067$ and $\chi^2_{\mathrm{Re}}=0.0068$, or about 12% rms disagreement per pixel with the measured data. The measure of reproducibility was $\xi^2_1=0.01$, or about 10% rms disagreement per pixel between the two best fits. To give some impression of the quality of the fit to which this numerical value corresponds, we present two slices from the 3D data set and the slices from the reconstruction that share this registration in the fast Fourier transform (FFT) array in Fig. 6. Figures 6(a) and 6(d) are separated by two rocking steps, with the latter being the 16th slice of 30. As expected for a real positive real-space object, the amplitude distribution in this slice is centrosymmetric in the reconstruction—Figs. 6(e) and 6(f)—while the data slice is not due to experimental complications inherent in finding the precise center of the diffraction pattern. Figure 7 shows three slices from the two best real-space reconstructions: slices 9, 15, and 21, with the better reconstruction on the left.

There is excellent agreement between the two reconstructions with the greatest difference near the center of the object [see Figs. 7(c) and 7(d)]. Each 2D slice in the reconstruction is a cut through the diffracting density that is perpendicular to the exit wave vector $\mathbf{k}_f$; we therefore refer to this as a "k_f view" of the density. This measurement was acquired with the sample mounted horizontally on the diffractometer, which was oriented so that the detector collected only diffraction from near the $(11\bar{1})$ Bragg peak, specified by the

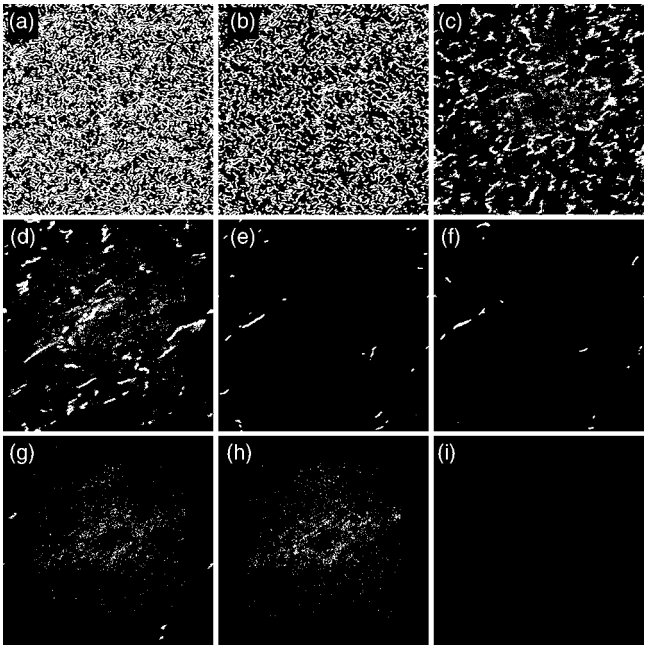

FIG. 4. Vortices in the 15th slice of the 3D reciprocal-space array as the fitting progresses. Each consecutive image is separated by 60 iterations starting with the 40th iteration in (a). Panels (a), (b), (d), (e), and (i) are during ER while (c), (f), (g), and (h) are during HIO. The vortices were detected by setting a threshold in the variation of the phase from one pixel to the next of 0.6 rad.

face-center-cubic Au lattice, with the (111) parallel to the surface normal of the sample. Since the experiment was conducted in a grazing exit geometry, the direction up and down the long edge of the page is the $\langle 11\bar{1}\rangle$ direction. The sample was expected to be a solid, uniform object, and yet the reconstruction shows significant internal density contrast. Examining Fig. 6, we estimate that there is significant signal up to about 6×10^{-3} Å^{-1}, giving a bound on the resolution in the plane: better than 1000 Å. If the same argument is ap-

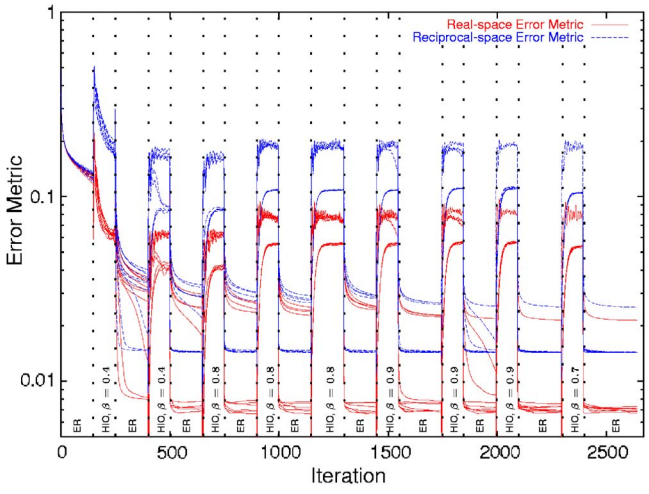

FIG. 5. (Color online) Real- and reciprocal-space error metric versus iteration for a typical fitting run. The metric rises to a higher value while HIO is applied. Note that rapid descents of the metric are common immediately after cycles of HIO.

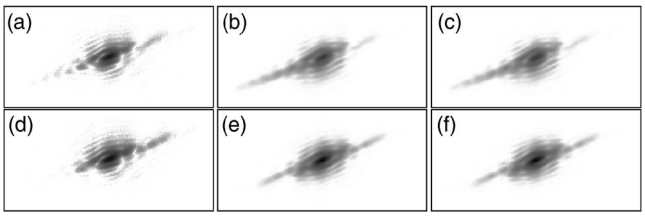

FIG. 6. 2D slices through the magnitude of the diffracted amplitude. Images (a) and (d) are the square root of the data, collected with a separation of two rocking steps, which is about 2×10^{-6} Å^{-1}. Images (b), (e), (c), and (f) are the magnitude of the reconstructed complex amplitude of the first and second best fits, respectively, in the same slices of the 3D FFT array. The images do not exactly correspond, in part because the calculated amplitude will always have a "centermost" slice, which is centrosymmetric, while the experiment failed to measure this data slice.

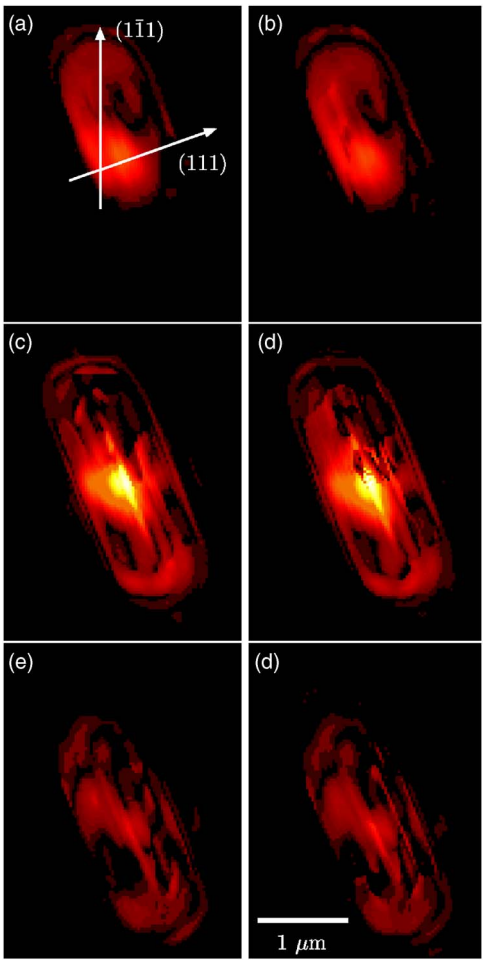

FIG. 7. (Color online) 2D slices through the reconstructed 3D density are shown for two fits. The slices are separated by 1.35 μm in the third direction, oriented out of the page. Both fits possess a bright region in the center of the real-space reconstruction, seen in (c) and (d), which is likely an artifact due to the partial coherence of the beam.

plied to the size of the FFT array, shown in Fig. 2, we find that a pixel is 385 Å.

We believe there are three distinct effects manifested in these reconstructions. First, the very high density near the center of the crystal [see Figs. 7(c) and 7(d)] is very similar to the expected effect of a partially coherent beam on the reconstruction.[21] Such an artifact might arise from imperfections in the Be window located 6 m upstream of the sample at beamline 33-ID-D. Imperfections, such as inclusions or surface roughness, in such an object may give rise to a "sharp" component of the mutual intensity function of the illumination, in turn leading to artifacts that manifest as a region of apparent high electron density in the reconstructed real-space object.[22]

Second, there are very fine lines of apparent low density appearing as dark stripes running diagonally from the top left to the bottom right of the density. If the crystal was suffering some residual defects from its formation, these might take the form of twinned regions,[23] the diffraction from which would not be captured by the detector in our experimental geometry. Such twinned regions ought to occur in (111) planes, which is exactly what we see in the reconstruction. Unfortunately, in the current experiment, the resolution—determined by the extent of reciprocal space captured in the detector—is about 50 nm, on the order of the expected size of the defects themselves. We note that the fine density modulations can be readily distinguished from the stripes caused by vortices. The vortices occur at random and have different configurations for every set of starting phases; the density modulations are highly reproducible from one fit to another, as Fig. 7 shows.

Finally, it is possible that some portions of the crystal are simply misoriented. This would be a sign of a highly strained crystal, the occurrence of which is not unreasonable given its formation from a film, bearing in mind that the film never surpassed the bulk melting point.

In several cases (not shown here), we relaxed our real-space positivity constraint and allowed the phase of the real-space object to go unconstrained during ER cycles. It was necessary to constrain the shape of the iterate during these cycles with a very tight support, lest the problem become underconstrained and thereby allow multiple solutions to exist. This loosening of the phase constraint in real space did not lead to significant evolution of the complex density the object, so we conclude that these features are not due to some artifact arising from an overconstrained problem.

V. CONCLUSION

The experiment described in this paper allowed the reconstruction of a crystal's 3D shape from its diffraction pattern while requiring only a small-angle scan of the sample with a 2D measurement at each angle. Even though a slightly strained sample should appear to have a complex density, thus allowing the recovery of the strain field, this was not supported by our result. Unfortunately, a highly strained particle may possess inclusions whose diffraction is not captured by the measurement, making the imaging less complete. Nevertheless, we have presented the recovery of a 3D density and shown that estimates with different starting points find the same solution to within the uncertainty of the fit to the measured data; i.e., the reproducibility is as good as the fit. The density so recovered possessed unexpected density contrast as well as artifacts due to the partial coherence of the incident beam. In the absence of a complete characterization of the beam, we have not attempted to remove this artifact. Some of the remaining modulation appears to be due to residual strain from the crystal formation, since other systems do not show this behavior.[18] We believe that the apparent density contrast is physical and not caused by the reconstruction procedure or a flaw in the experiment. When using an iterative technique involving a nonlinear operation, one is naturally concerned about the possible effects of noise in the measurement upon the reconstruction, but simulations of noisy CXD data have not shown such reproducible artifacts.[18,19]

ACKNOWLEDGMENTS

This research was supported by the NSF under Grant No. DMR 03-08660. The UNICAT facility at the Advanced Photon Source (APS) is supported by the University of Illinois at Urbana-Champaign, Materials Research Laboratory (U.S. DOE Contract No. DEFG02-91ER45439, the State of Illinois-IBHE-HECA, and the NSF), the Oak Ridge National Laboratory (U.S. DOE under contract with UT-Battelle LLC), the National Institute of Standards and Technology (U.S. Department of Commerce), and UOP LLC. The APS is supported by the U.S. DOE, Basic Energy Sciences, Office of Science under Contract No. W-31-109-ENG-38. Scanning electron microscope work was carried out in the Center for Microanalysis of Materials, University of Illinois.

*Present affiliation: ARC Centre of Excellence for Coherent X-ray Science, School of Physics, The University of Melbourne, Melbourne, Australia.
†Present address: Advanced Light Source, Berkeley, CA, USA.
‡Present address: HASYLAB, DESY, Hamburg, Germany.

[1] J. R. Fienup, Opt. Lett. **3**, 27 (1978).
[2] R. W. Gerchberg and W. O. Saxton, Optik (Stuttgart) **35**, 237 (1972).
[3] R. P. Millane, J. Opt. Soc. Am. A **7**, 394 (1990).
[4] R. Barakat and G. Newsam, J. Math. Phys. **25**, 3190 (1984).
[5] R. H. T. Bates, Optik (Stuttgart) **61**, 247 (1982).
[6] Y. M. Bruck and L. G. Sodin, Opt. Commun. **30**, 304 (1979).
[7] D. Sayre, Acta Crystallogr. **5**, 843 (1952).
[8] J. Miao, D. Sayre, and H. N. Chapman, J. Opt. Soc. Am. A **15**, 1662 (1998).
[9] R. P. Millane, J. Opt. Soc. Am. A **13**, 725 (1996).
[10] J. Miao, P. Charalambous, J. Kirz, and D. Sayre, Nature (London) **400**, 342 (1999).

[11] I. K. Robinson, I. A. Vartanyants, G. J. Williams, M. A. Pfeifer, and J. A. Pitney, Phys. Rev. Lett. **87**, 195505 (2001).
[12] J. Miao, T. Ishikawa, B. Johnson, E. H. Anderson, B. Lai, and K. O. Hodgson, Phys. Rev. Lett. **89**, 088303 (2002).
[13] G. J. Williams, M. A. Pfeifer, I. A. Vartanyants, and I. K. Robinson, Phys. Rev. Lett. **90**, 175501 (2003).
[14] S. Marchesni, H. N. Chapman, S. P. Hau-Riege, R. A. London, A. Szoke, H. He, M. R. Howells, H. Padmore, R. Rosen, J. C. H. Spence, and U. Weierstall, Opt. Express **11**, 2344 (2003).
[15] V. Elser, J. Opt. Soc. Am. A **20**, 40 (2003).
[16] H. H. Bauschke, P. L. Combettes, and D. R. Luke, Proceedings of the IEEE International Conference on Image Processing, Rochester, NY, 2002, vol. 2, p. 841 (2002).
[17] J. R. Fienup, Appl. Opt. **21**, 2758 (1982).
[18] G. J. Williams, Ph.D. thesis, University of Illinois at Urbana-Champaign, 2005.
[19] G. J. Williams, M. A. Pfeifer, I. A. Vartaniants, and I. K. Robinson, Proc. SPIE **5562**, 208 (2004).
[20] J. H. Seldin and J. R. Fienup, J. Opt. Soc. Am. A **7**, 412 (1990).
[21] I. A. Vartanyants and I. K. Robinson, J. Phys.: Condens. Matter **13**, 10593 (2001).
[22] I. A. Vartanyants and I. K. Robinson, Opt. Commun. **222**, 29 (2003).
[23] H. W. Hayden, W. G. Moffat, and J. Wulff, *Structure and Properties of Materials III* (Wiley, New York, 1965).